In situ lower crustal accretion by melt sill injection revealed by seismic layering

Peng Guo[1,*], Satish C. Singh[2,*], Venkata A. Vaddineni[2], Ingo Grevemeyer[3] and Erdinc Saygin[1,4]

1. Deep Earth Imaging Future Science Platform, Commonwealth Scientific and Industrial Research Organisation (CSIRO), Kensington 6151, Australia; peng.guo@csiro.au

2. Laboratoire de Géosciences Marines, Institut de Physique du Globe de Paris, Paris 75005, France; singh@ipgp.fr

3. GEOMAR Helmholtz Centre for Ocean Research, D-24148 Kiel, Germany

4. Department of Physics, School of Physics, Mathematics and Computing, Faculty of Engineering and Mathematical Sciences, University of Western Australia, Crawley 6009, Australia

Oceanic crust is formed at mid-ocean spreading centres by a combination of magmatic, tectonic and hydrothermal processes[1-3]. The crust formed by magmatic process consists of an upper crust generally composed of basaltic dikes and lava flows and a lower crust presumed to mainly contain homogeneous gabbro[3] whereas that by tectonic process can be very heterogeneous and may even contain mantle rocks[4,5]. Although the formation and evolution of the upper crust are well known from geophysical[6-9] and drilling results[10,11], those for the lower crust remain a matter of debate. Using a full waveform inversion method applied to wide-angle seismic data, here we report the presence of layering in the lower oceanic crust formed at the slow spreading Mid-Atlantic Ridge, ~7-12 Ma in age, revealing that the lower crust is formed mainly by in situ cooling and crystallisation of melt sills at different depths by the injection of magma from the mantle. These layers are 400-600 m thick with alternate high and low velocities, with ± 100-200 m/s velocity variation, and cover over a million-year old crust, suggesting that the crustal accretion

by melt sill intrusions beneath the ridge axis is a stable process. We also find that the upper crust is ~400 m thinner than that from conventional travel-time analysis. Taken together, these discoveries suggest that the magmatism plays more important roles in the crustal accretion process at slow spreading ridges than previously realised, and that in-situ lower crustal accretion is the main process for the formation of lower oceanic crust.

Our study area lies in the equatorial Atlantic Ocean (Fig. 1). The equatorial Atlantic Ocean opened during the Late Jurassic, sundering Gondwanaland and separating northern South America from Africa. After break-up, seafloor spreading occurred along the slow spreading Mid-Atlantic Ridge, forming up to 120 Ma old oceanic crust. Half spreading rate to the south of the equator remained in the order of ~16 mm/year[12] over the last 20 Myr.

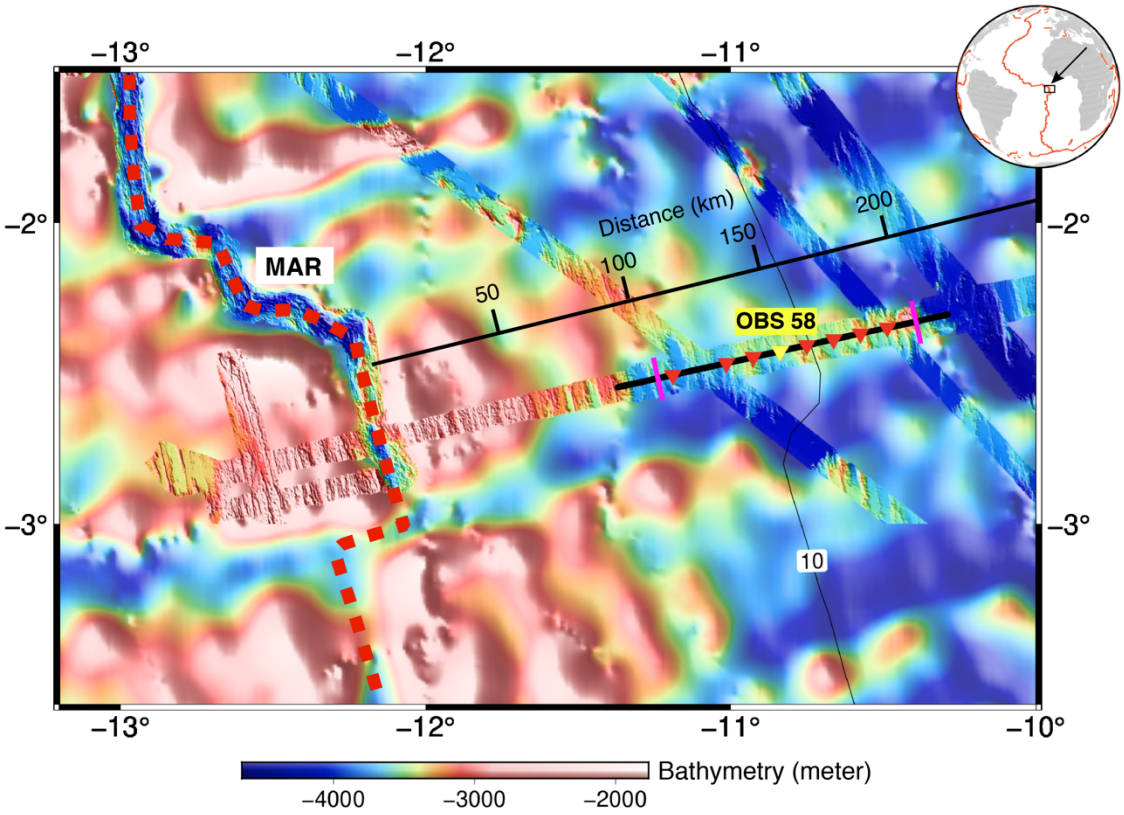

Fig. 1: Study Area: The ocean bottom seismometer (OBS) seismic survey near the Mid-Atlantic Ridge (MAR) in the equatorial Atlantic Ocean. The dashed red line refers to the MAR, and the triangles show the locations of the OBSs used for this study. OBS 58 (yellow triangle) is labelled, with the seismograms shown in Fig. 3. The bold black line passing through OBSs shows the part of shot profile used, and the two pink bars indicate the boundaries of the seismic images shown in Fig. 2. The thin black line and numbers indicate the distance from the MAR. The contour labelling 10 indicates the 10 Ma lithospheric age. See the inset map for the location of the study area.

In 2017, wide-angle seismic data were acquired aboard the German R/V Maria S. Marian. An air gun array with a total volume of 5440 cubic inch was fired at ~400 m interval, which was recorded on ocean bottom seismometers (OBSs) deployed at a spacing of 10 to 20 km on the seafloor. The crustal (Pg), mantle arrivals (Pn) and wide-angle reflections from the Moho (PmP) were used to obtain the large-scale P-wave velocity structures[13]. Here, we use a part of these data (8 OBSs) where the OBS spacing was dominantly ~10 km (Fig. 1), covering ~7 to 12 Ma old seafloor. Fig. 2a shows the velocity model obtained using the travel-time tomography[13] (see Methods), which was used as the starting velocity model for the full waveform inversion[14,15] (FWI, see Methods). The crustal thickness in the study area is 5.8 ± 0.2 km[13]. As expected, the tomographic velocity model contains only the large-scale velocity structures but clearly showing a high velocity gradient upper crust down to ~2.4 km below the basement underlain by a low velocity gradient lower crust.

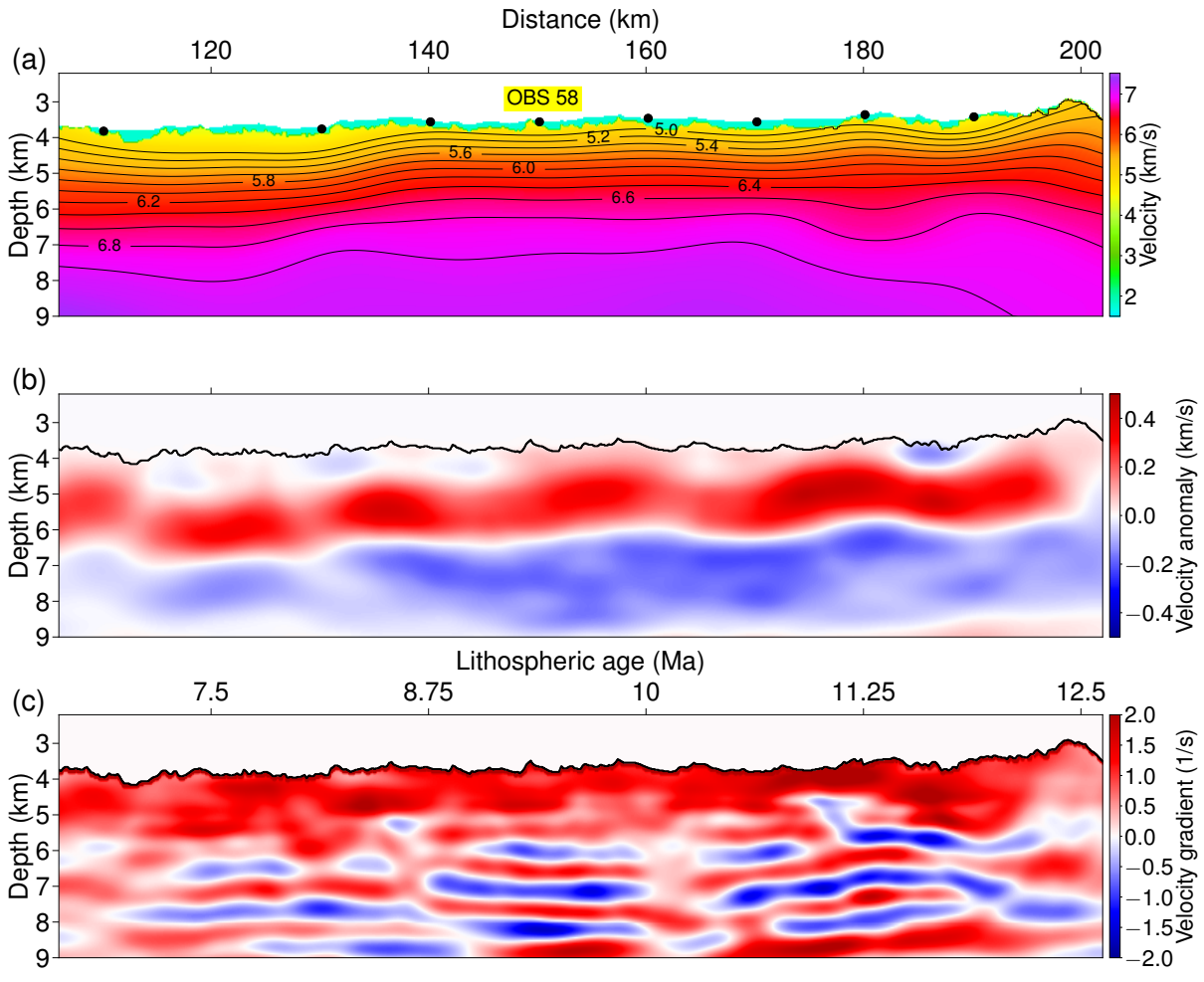

Fig. 2: Velocity Models: (a) The tomographic seismic velocity model[13] serves as the starting model for the FWI, (b) the velocity anomaly (the difference between the velocity models from FWI and tomography) from the trace-normalised FWI[14], and (c) the vertical velocity gradient (the derivative of velocity with respect to depth) from the 'true amplitude' FWI[15]. Black dots in (a) mark the OBS locations. The velocity contours are from 5 to 7 km/s with an increment of 0.2 km/s. The coloured parts in (b) and (c) start from the basement (the top of Layer 2). The lithospheric age in (c) is calculated using a spreading rate of 16 mm/year[12]. More images of the oceanic crustal velocity models from FWI can be found in Figs. S3 and S4. The horizontal distance starts with 0 km from the MAR.

Fig. 2b shows the velocity anomaly obtained using the trace-normalised FWI[14] (see Methods), which indicates an overall increase in the velocity (Figs. 2b, S3) (positive velocity anomaly) above 6-7 km depth and a decrease in velocity (negative velocity anomaly) below this depth, suggesting that the velocity in the upper crust is 200-400 m/s higher than those obtained from the tomographic method and is 100-300 m/s lower in the lower crust. Starting from this velocity model, we performed the true-amplitude FWI[15] (see Methods) (Figs. 2c, S4). There are alternate high and low velocity layers in the lower crust below ~6 km depth in the vertical velocity gradient image (Figs. 2c, 4a). The synthetically calculated data after the FWI show a much better match to the crustal Pg arrivals of the field data than those from the tomographic model (Figs. 3, S7-S10).

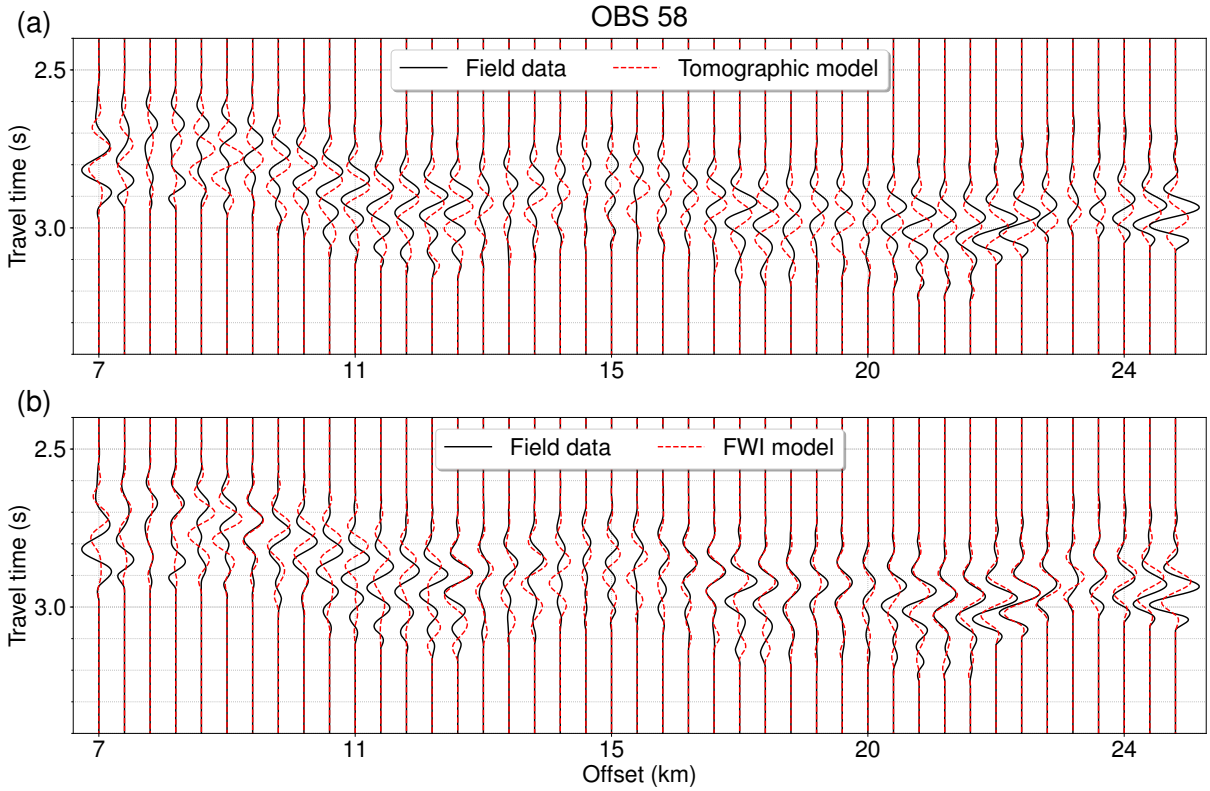

Fig. 3: Data comparison for OBS 58: (a) The field data (black) and the synthetic waveform (red) using the tomographic model (Fig. 2a), and (b) the field data (black) and the synthetic waveform (red) using the true-amplitude FWI model (Fig. S4a). Seismic waveforms from

more OBSs can be found in Figs. S7-S10. A reduced travel time of 7 km/s velocity was applied to both the field and synthetic data for plotting purpose.

In order to make sure that these results from inverting Pg arrivals represent real crustal features, we performed extensive simulated inversion tests with different structures embedded in the model. Synthetic data were computed and then were inverted using the same parameters as the field data inversion (see Methods, Figs. S12-S24). These tests suggest that the layered velocity model in the lower crust is required by the data, and hence they are real structures in the sub-surface. As the dominant frequency in the data is 3.5-10 Hz, the dominant wavelength is 700-1500 m for a velocity of 6.8 km/s, indicating that the vertical resolution in the lower crust is ~ 400 m[15], hence the structures we observed are well resolved.

One-dimensional velocity profiles (Figs. 4a, S5-S6) show three distinct features: (1) a layer with a much higher vertical velocity gradient than that of the tomographic model from the basement down to ~1.2 km depth, where the velocity linearly increases from an average of ~4.8 km/s at the top to 6.2 km/s at its base, (2) an underlying medium velocity gradient layer of 600-800 m thickness, with the velocity increasing to ~6.6 km/s, and (3) alternating high and low velocity layers (400-600 m thick) with a velocity variation of ±100 - 200 m/s in the lower crust extending over 10-20 km distance along the profile.

The upper high velocity gradient layer is probably associated with the high velocity gradient generally observed at the lava flow-dike (layer 2A/2B) boundary[16], where the rapid velocity increase mainly comes from the collapsing and filling of cracks/pores from lithostatic pressure and hydrothermal precipitation[16,17]. A recent tomographic study using ultra-long streamer data indicates that this boundary lies at 600 - 800 m below basement for ~ 7–12 Ma[9], suggesting a shallower 2A/2B transition than our results. However, these authors found

111 the lava flow-dike boundary at ~ 900 m below the seafloor beneath the ridge axis[9]. The
112 relatively limited offset and low resolution of the tomographic inversion might be the cause
113 of this discrepancy.

114 Generally, the upper and lower crust boundary is defined by a change in the vertical velocity
115 gradient; high velocity gradient in the upper crust with very low gradient in the lower
116 crust[3,8,17]. Using this definition, the upper crust-lower crust boundary will be at 2.2-2.4 km
117 below basement in the tomographic model and at 1.8-2.0 km in the FWI results (Figs. 4a, S5-
118 S6), suggesting that the upper crust is ~400 m thinner (20%) than that based on the travel
119 time analysis, but is consistent with the average thickness of 1.9 km for old (> 7.5 Ma) upper
120 crust from slow-spreading ridges[3]. Consequently, the lower crust (Layer 3), which mainly
121 consists of gabbro, would be much thicker, suggesting that magmatic process may play a
122 more important role in crustal accretion than previously realised[2]. The average velocity at the
123 top of the lower crust is 6.6 km/s, which is well within the range of 6.56-6.7 km/s estimated
124 from historic surveys[3].

125 The alternating high and low velocity layers below ~2 km depth from basement in the lower
126 crust could be explained by the presence of (1) gabbro sills within emplaced mantle
127 peridotite[4,5,18], (2) hydrothermal alteration[19], or (3) multiple injection and freezing of melt
128 sills of different types of melt in the lower crust beneath the ridge axis[20,21].

129 The observation of clear wide-angle Moho reflections (PmP, Fig. S2) on all the OBSs
130 requires the presence of a distinct Moho at ~ 5.8 km below the basement[13], indicating that the
131 Moho is a petrological boundary separating the gabbroic crust above the mantle peridotite.
132 Furthermore, the tomographic results indicate that velocity in the lower crust increases from
133 ~ 6.6 km/s at 2 km below the basement to ~ 7 km/s just above the Moho, suggestive of a
134 gabbroic origin. The velocity in the mantle just below the Moho is ~ 8 km/s, confirming the

presence of mantle peridotite[13]. Additionally, the velocities in the high velocity layers of lower crust are too low to represent serpentinised peridotite. Taken together, these results suggest that the observed lower crustal seismic layering is not due to the presence of gabbro sills in uplifted mantle peridotite.

Previous seismic investigation[19] has imaged a 150-200 m thick low-velocity zone above the roof of the axial melt lens (AML), which was interpreted to be formed from enhanced hydrothermal alteration[19]. Therefore, the topmost low velocity layer might be associated with this enhanced hydrothermal circulation.

Multiple magma lenses in the lower crust have been recently discovered through modern seismic surveys at the fast[22-24] and intermediate spreading ridges[25,26], supporting the idea of in-situ magma intrusion and crystallisation in the lower crust. However, no such secondary lower crustal melt sills have been observed beneath slow spreading ridges, although low velocity anomalies have been reported in the lower crust, suggestive of the presence of partial melt (mush)[8,27]. The absence of melt sill evidence beneath slow spreading ridges could be either due to rough seafloor hindering seismic imaging or because of low velocity contrasts between the host mush and the injected melt sills.

The layering in the lower crust has been observed in exposed ophiolites. In the Oman ophiolite, which is a representative of fast spreading crust, thin layers (cm to 100 m) of alternating strata rich in mafic minerals (olivine and clinopyroxene) and plagioclase have been observed[20,21,28]. The analysis of these layers suggests that the lower crust could be formed by cooling and crystallisation of melt sills in situ (the sheeted sill model[20,21]). In the Bay of Islands ophiolite, a representative of slow spreading environment, layers with thickness of several hundred meters to a kilometer have been observed[29].

158 A more than 1500-m of the lower crustal gabbro was drilled during the Ocean Drilling
159 Program Hole 735B[30,31], containing several layered units of >250 m thickness. Analysis of a
160 geochemical unit in the lower gabbro[31] suggests that it constitutes of a single magma
161 reservoir but is separated in two parts. The lower part is formed by a stack of repeated
162 recharge of primitive thin melt sills, whereas the upper part consists of a homogeneous
163 evolved magma mush formed by upward reactive porous flow, progressive differentiation
164 and accumulation[31,32]. This process would lead to a layering in the lower crust, containing
165 olivine-rich gabbro and troctolites at the base with a distinct boundary separating more
166 evolved olivine and olivine-bearing gabbro with decreasing olivine and increasing
167 plagioclase[31].

168 Observations from IODP/ODP drilling and ophiolites[28-33] indicate that the lower crustal
169 gabbroic rocks are mainly composed of olivine (Ol), clinopyroxene (Cpx), and plagioclase
170 (Pl), with seismic velocities $V_{Ol} > V_{Cpx} > V_{Pl}$ (Table S1), where V represents the velocity.
171 Rocks rich in Ol and Cpx, indicative of more primitive melt, would have higher velocities,
172 whereas those of more evolved rocks rich in Pl would have relatively lower velocities[33,34].
173 Using the Voigt-Reuss-Hill averaging method (See Methods), we computed the P-wave
174 velocities for different gabbro compositions from the Hole 735B, and found that the velocity
175 of the gabbro varies from 6.6 km/s to 7.1 km/s (Table S2), for 10% - 20% changes in Ol/Cpx
176 and Pl contents. Therefore, high-velocity layers may contain gabbroic rocks with relatively
177 high Ol/Cpx concentration (usually >10%) such as Ol and Ol-rich gabbro; low-velocity layer
178 may be rich in rocks with low Ol/Cpx (<10%) and high Pl contents, such as Ol-bearing
179 gabbro.

180 The observed lower crustal layering extends over 10-20 km horizontal distance along the
181 profile (Fig. 2c), suggesting that the crustal accretion process by sill injection is stable for up

to a million year. A sustained melt supply and a relatively stable crustal accretion process can indeed be a general phenomenon at slow-spreading ridges, especially when the process is not interrupted by the presence of detachment faults[4,5], which seems to be the case in our study region; otherwise the layered structure would be more discontinuous. Further, bathymetric data show simple abyssal hill fabrics indicating a normal mode of seafloor spreading. A robust and stable magma supply is also consistent with the estimated thick lower crust. It is also possible that these interpreted frozen sills are thinner and shorter, but our data do not have the resolution to image them, and higher resolution seismic data would be required.

Our discovery of layering in the lower crust at the slow-spreading MAR provides important implications for the crustal accretion process, indicating that melt sills in the lower may be more prevalent than previously realised. Fig. 4b shows a schematic diagram about the geometry of the melt lens and the oceanic crust. The discovery of stacked-layering off axis firmly confirms that the lower oceanic crust is formed by the crystallisation of melt sills in situ by multiple injections of upwelling magma from the mantle[21], not just in the upper axial melt lens then subsiding to greater depths as suggested by the gabbro glacier model[35]. The alternating high and low velocities indicates the progressive extraction and assimilation of cyclically replenished melts. The high-velocity layers are likely to be formed from primitive melt intrusions at the base of a magma reservoir, whereas the low-velocity layers can be produced by the fractional crystallisation and accumulation of more-evolved, upward-migrated melt residue (mush). In situ crystallisation requires extensive seawater circulation down to the Moho depth along the sides of crystal-rich mush zone beneath the magma chambers for cooling[34], which can be provided through well-developed faults in the slow-spreading environment[31]. Moreover, the hydrothermal activities and the magmatic reaction with host rocks could lead to remelting and assimilation, altering the petrological constituents of igneous rocks[31,32], hence changing the rock properties further.

Our results provide the first seismic image for a layered lower oceanic crust away from spreading centres. We suggest that, similar to continental lower crust[36], the oceanic lower crust is generally composed of high and low velocity layers, in contrast to the presumed homogeneous gabbroic lower crust or the presence of mantle peridotite in the lower crust. The existence of layering in the lower crust provides a strong evidence that magmatism is the main driving force for the crustal accretion process at slow spreading mid-oceanic ridges, and that the normal oceanic lower crust is primarily formed by in situ cooling and crystallisation of cyclic magma upwelling from the upper mantle. Furthermore, the amount of melt produced in the mantle should be much larger, and hence the mantle must be much hotter or melt extraction is much more efficient beneath slow spreading ridges than previously realised.

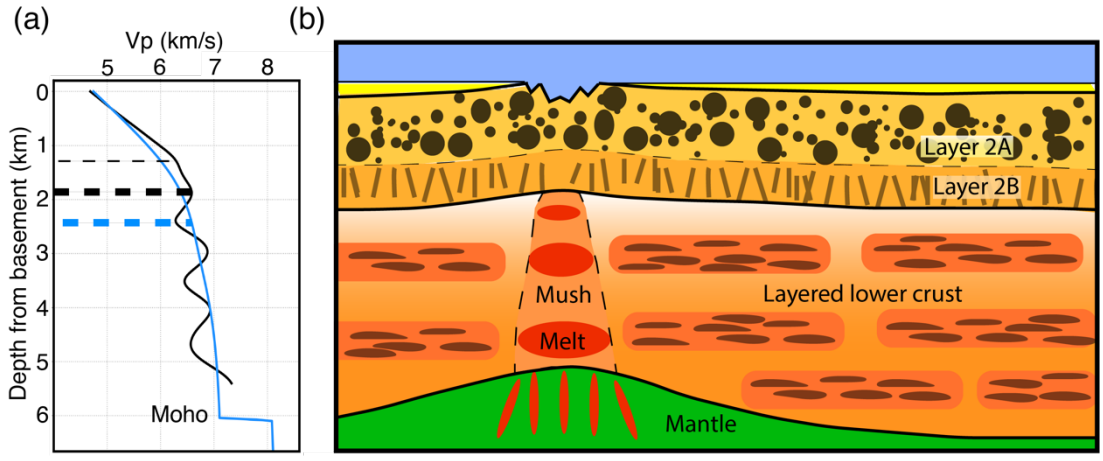

Fig. 4: Layering in the lower crust: (a) One-dimensional velocity-depth profiles at the distance of 182 km from the MAR, derived from tomography (blue) and FWI (black), respectively. The thin dashed black line is the interpreted boundary of Layer 2A/2B from the FWI model; the bold dashed blue and black lines indicate the boundaries of Layer 2/3 from the tomographic and the FWI models, respectively. We invert the velocity model from FWI down to a maximum 9 km depth (~5.4 km from basement at distance 182 km), because of

potential Moho reflection interference for greater depths (Figs. S23, S24). (b) A schematic diagram illustrating the oceanic crustal structure at the MAR and away from the ridge axis.

References

1. Morgan, J. P., & Chen, Y. J. The genesis of oceanic crust: Magma injection, hydrothermal circulation, and crustal flow. *J. Geophys. Res. Solid Earth* **98**, 6283-6297 (1993).
2. Cannat, M. et al. Thin crust, ultramafic exposures, and rugged faulting patterns at the Mid-Atlantic Ridge (22–24 N). *Geology* **23**, 49-52 (1995).
3. Christeson, G. L., Goff, J. A., & Reece, R. S. Synthesis of Oceanic Crustal Structure From Two-Dimensional Seismic Profiles. *Rev. Geophys*. **57**, 504-529 (2019).
4. Cannat, M. Emplacement of mantle rocks in the seafloor at mid‐ocean ridges. *J. Geophys. Res. Solid Earth* **98**, 4163-4172 (1993).
5. Grevemeyer, I., Hayman, N.W., Peirce C., Schwardt M., Van Avendonk H.J.A., Dannowski A., Papenberg C. Episodic magmatism and serpentinized mantle exhumation at an ultraslow-spreading centre, *Nat. Geosci.* **11**, 444-448 (2018).
6. Harding, A. J., Kent, G. M., & Orcutt, J. A. A multichannel seismic investigation of upper crustal structure at 9° N on the East Pacific Rise: Implications for crustal accretion. *J. Geophys. Res. Solid Earth* **98**, 13925-13944 (1993).
7. Toomey, D. R., Solomon, S. C., & Purdy, G. M. Tomographic imaging of the shallow crustal structure of the East Pacific Rise at 9° 30′ N. *J. Geophys. Res. Solid Earth* **99**, 24135-24157 (1994).

8. Seher, T. et al. Crustal velocity structure of the Lucky Strike segment of the Mid‐Atlantic Ridge at 37° N from seismic refraction measurements. *J. Geophys. Res. Solid Earth* **115**, B03103 (2010).
9. Audhkhasi, P., & Singh, S. C. Seismic Structure of the Upper Crust From 0–75 Ma in the Equatorial Atlantic Ocean on the African Plate Using Ultralong Offset Seismic Data. *Geochem. Geophys. Geosyst.* **20**, 6140-6162 (2019).
10. Hyndman, R. D., Langseth, M. G., & Von Herzen, R. P. Deep Sea Drilling Project geothermal measurements: a review. *Rev. Geophys* **25**, 1563-1582 (1987).
11. Wilson, D. S. et al. Drilling to gabbro in intact ocean crust. *Science* **312**, 1016-1020 (2006).
12. Müller, R. D., Sdrolias M., Gaina C., and Roest W. R. Age, spreading rates, and spreading asymmetry of the world's ocean crust, *Geochem. Geophys. Geosyst.* **9**, Q04006 (2008).
13. Vaddineni, V.A., Singh, S.C., Grevemeyer, I., Audhkhasi P., & Papenberg C. Evolution of the Crustal and upper Mantle seismic structure from 0 – 27 Ma in the equatorial Atlantic Ocean at 2º 43'S. Submitted to *J. Geophys. Res. Solid Earth*.
14. Wang, Z., Singh, S. C., & Noble, M. True-amplitude versus trace-normalized full waveform inversion. *Geophys. J. Int.* **220**, 1421-1435 (2020).
15. Shipp, R. M., & Singh, S. C. Two-dimensional full wavefield inversion of wide- aperture marine seismic streamer data. *Geophys. J. Int.* **151**, 325-344 (2002).
16. Detrick, R. S. et al. Seismic structure of the southern East Pacific Rise. *Science* **259**, 499-503 (1993).
17. Grevemeyer, I., Ranero, C.R., and Ivandic, M. Structure of oceanic crust and serpentinization at subduction trenches: *Geosphere*, 14, 395–418 (2018).

18. Xu, M., Zhao, X., & Canales, J. P. Structural variability within the Kane oceanic core complex from full waveform inversion and reverse time migration of streamer data. *Geophys. Res. Lett.* **47**, e2020GL087405 (2020).

19. Singh, S. C., Collier, J. S., Harding, A. J., Kent, G. M., & Orcutt J. A. Seismic evidence for a hydrothermal layer above the solid roof of the axial magma chamber at the southern East Pacific Rise. *Geology* **27**, 219-222 (1999).

20. Boudier, F., Nicolas, A., & Ildefonse, B. Magma chambers in the Oman ophiolite: fed from the top and the bottom. *Earth Planet. Sci. Lett.* **144**, 239-250 (1996).

21. Kelemen, P. B., Koga, K., & Shimizu, N. Geochemistry of gabbro sills in the crust-mantle transition zone of the Oman ophiolite: Implications for the origin of the oceanic lower crust. *Earth Planet. Sci. Lett.* **146**, 475-488 (1997).

22. Canales, J. P. et al. Network of off-axis melt bodies at the East Pacific Rise. *Nat. Geosci.* **5**, 279-283 (2012).

23. Marjanović M. et al. A multi-sill magma plumbing system beneath the axis of the East Pacific Rise. *Nat. Geosci.* **7**, 825-829 (2014).

24. Arnulf, A. F., Singh, S. C., & Pye, J. W. Seismic evidence of a complex multi- lens melt reservoir beneath the 9° N Overlapping Spreading Center at the East Pacific Rise. *Geophys. Res. Lett.* **41**, 6109-6115 (2014).

25. Carbotte, S. M. et al. Stacked sills forming a deep melt-mush feeder conduit beneath Axial Seamount. *Geology* **48**, 693-697 (2020).

26. Canales, J. P., Nedimović, M. R., Kent, G. M., Carbotte, S. M., & Detrick R. S. Seismic reflection images of a near-axis melt sill within the lower crust at the Juan de Fuca ridge. *Nature* **460**, 89-93 (2009).

27. Dunn, R. A., Lekić, V., Detrick, R. S., & Toomey, D. R. Three‐dimensional seismic structure of the Mid‐Atlantic Ridge (35° N): Evidence for focused melt supply and lower crustal dike injection. *J. Geophys. Res. Solid Earth* **110**, B09101 (2005).
28. VanTongeren, J. A., Kelemen, P. B., & Hanghøj, K. Cooling rates in the lower crust of the Oman ophiolite: Ca in olivine, revisited. *Earth Planet. Sci. Lett.* **267**, 69-82 (2008).
29. Casey, J. F., & Karson, J. A. Magma chamber profiles from the Bay of Islands ophiolite complex. *Nature* **292**, 295-301 (1981).
30. Natland, J. H., Dick, H. J. B., Miller, D. J., & Von Herzen, R. P. Velocity structure of the lower oceanic crust: results from Hole 735B, Atlantic II Fracture Zone. In *Proc. ODP, Sci. Results* **176**, 1-71 (College Station, Tex.: Ocean Drilling Program. 2001)
31. Boulanger, M. et al. Magma reservoir formation and evolution at a slow-spreading center (Atlantis Bank, Southwest Indian Ridge). *Front. Earth Sci.* **8**, 554598 (2020).
32. Lissenberg, C. J., MacLeod, C. J., Howard, K. A., & Godard, M. Pervasive reactive melt migration through fast-spreading lower oceanic crust (Hess Deep, equatorial Pacific Ocean). *Earth Planet. Sci. Lett.* **361**, 436-447 (2013).
33. Carlson, R. L., & Jay Miller, D. Influence of pressure and mineralogy on seismic velocities in oceanic gabbros: Implications for the composition and state of the lower oceanic crust. *J. Geophys. Res. Solid Earth* **109**, B09205 (2004).
34. Maclennan, J., Hulme, T., & Singh, S. C. Thermal models of oceanic crustal accretion: Linking geophysical, geological and petrological observations. *Geochem. Geophys. Geosyst.* **5**, Q02F25 (2004).
35. Quick, J. E., & Denlinger, R. P. Ductile deformation and the origin of layered gabbro in ophiolites. *J. Geophys. Res. Solid Earth*, 98, 14015-14027 (1993).
36. Singh, S. C., & McKenzie, D. Layering in the lower crust. *Geophys. J. Int.* **113**, 622-628 (1993).

Methods

Data acquisition

The field OBS data was acquired during the LITHOS-iLAB cruise in November-December 2017 onboard the Germain R/V Maria S. Merian to study the upper lithosphere from 0-50 Ma in the study region[37]. A total of 71 instruments consisting of 55 ocean bottom seismometers (OBSs) and 16 ocean bottom hydrophones (OBHs) were deployed along a 1100-km long transect with a variable spacing of 10-20 km to record wide-angle refractions and reflection arrivals. The majority of the profile (~1000 km) lies on the African Plate (0-50 Ma) and crosses the ridge-axis on to the South American Plate (0-2 Ma) for ~75 km. All OBSs were equipped with a hydrophone (measuring pressure) and three geophones (measuring vertical and horizontal displacements) whereas the OBHs measured only the pressure. The data was sampled at 250 Hz. The active seismic source used in the survey comprised of 6 G-gun clusters (12 guns) configured as two sub-arrays with a total volume of 5440 cubic inch, which was towed at 7.5 m in depth and fired every ~400 m along the profile. The relatively large shot spacing was chosen to reduce the noise from neighbouring shots and hence enhancing the signal-to-noise ratio for farther offsets. We used a part of these data (8 OBSs, pressure component) where the OBS spacing was dominantly ~10 km covering 7-12 Ma old oceanic crust (Fig. 1 and Fig. S1).

Data pre-processing

We limit the data pre-processing to a minimum to keep the waveform information, including a zero-phase bandpass filtering of 3.5 - 10 Hz, and 3D to 2D transformation[15,38] (multiplying the amplitudes of field data by $\sqrt{t}$, where t is the two-way travel-time, and convolving with

342 $1/\sqrt{t}$) because 2D elastic wave equation modelling was used for simulating seismic data
343 recorded in a 3D earth. A predictive deconvolution was applied to suppress the bubble effects
344 from the air gun sources. Clear crustal turning waves (Pg) with high signal-to-noise ratio can
345 be observed starting from offsets (source-receiver distance) ± 6 - 8 km, up to offsets of ± 20 -
346 26 km, followed by wide-aperture Moho reflection (PmP) and upper mantle refraction (Pn) at
347 the far offsets. An OBS gather (OBS 58) is shown in Fig. S2, with Pg, PmP, and Pn arrivals
348 labelled.

349 **Travel time tomography**

350 Travel time tomography[13,39] was first applied to the OBS gathers for estimating a P wave
351 velocity model (Fig. 2a). Travel times of Pg, PmP and Pn were hand-picked with an
352 uncertainty of 30 ms. Tomography was carried out through a linearised approach by updating
353 velocity models iteratively[39]. At each iteration, a ray-tracing algorithm with a hybrid of graph
354 (shortest path) method and ray bending for further refinements was used for forward
355 modelling of travel times; the model update (the partial derivatives of travel times to the
356 model parameters) was obtained by least-squares penalties on the data misfit, together with
357 smoothing and damping for regularising the inversion problem[39].

358 The velocity model from travel time tomography gives very good travel-time fit for the first
359 arrival[13]. Since the travel time is mainly sensitive to large-scale velocity structures, the
360 tomographic velocity model contains few details for the oceanic crust. The first arrival, Pg,
361 rays penetrate down to ~3 km below the seafloor, thus the velocity in the lower crust is
362 mainly determined using PmP arrivals, which is poorly constrained because of the trade-off
363 between the lower crustal velocity and the Moho depth. Details of the travel-time tomography
364 can be found in Vaddineni et al (2020)[13].

365

366 **Full waveform inversion (FWI)**

367 FWI is the current state-of-the-art technique for high-resolution subsurface imaging[15,37,38].
368 We adopted the approach of time-domain finite-difference elastic FWI[15] for improving the
369 tomographic model. Unlike travel-time tomography that relies on minimizing the travel time
370 from high-frequency approximated ray-tracing[39], the FWI is based on minimising the
371 difference between the observed and synthetic seismic waveforms, with a numerical solution
372 of the elastic wave-equation for realistic simulation of seismic wave propagation in the
373 frequency band of interest[15,38]. For the numerical implementation, a gradient-based linearised
374 inversion approach is used for updating the velocity model iteratively, with the gradients of
375 the data misfit to model parameters efficiently calculated by the adjoint method from cross-
376 correlation of the forward and adjoint wavefields[15,38].

377 The capability of recovering high-resolution crustal images using the FWI comes from the
378 fact that the amplitudes and waveforms of the recorded wavefield are more sensitive to fine-
379 scale geological features than travel time. It also has the potential of being sensitive to crustal
380 structures at greater depth than travel-time tomography, with the increased depth coverage
381 attributed to a wavelength of ~1.2 km from finite-bandwidth waveform (a dominant
382 frequency of 6 Hz with ~6.8 km/s P-wave velocity in the lower crust) rather than a high-
383 frequency approximated ray path. Furthermore, other wide-angle arrivals, e.g. weak
384 reflections from the lower crust, are included in the waveforms.

385 Although the tomographic inversion using ray-trace modelling has converged with good
386 travel-time fit[13], large waveform difference can be observed between the field data and the
387 synthetic seismograms from wave-equation modelling (Fig. 3, Figs. S7-S10). Hence, we
388 employed a multi-stage strategy for obtaining the final model. In the first stage of FWI, the

389 tomographic model was used as the starting model. A trace-normalised FWI[14] was applied,
390 where the amplitudes of each trace within a common OBS gather were normalised by the
391 norm-2 of the trace itself. This may be considered as a bridge between tomography and
392 classic FWI using 'true amplitude' waveform: the influence of amplitude-versus-offset is
393 removed by trace-by-trace normalisation and the inversion mainly focuses on fitting the
394 phase information simulated from elastic wave-equation modelling. From trace-normalised
395 FWI, we were able to obtain an improved crustal model (Fig. S3). In the second stage, we
396 performed a true-amplitude FWI[15,38], with the waveform misfit between field and synthetic
397 data being the objective function for minimisation. The inversion was carried out using a top-
398 down approach: we inverted first for the relatively shallow structures, which were
399 constrained by near-to-intermediate source-receiver offset ranges (from ± 6-8 km up to ±15
400 km offsets) of crustal Pg arrivals, then far-offset arrivals were included for estimating the
401 deeper crustal model. The updated velocity model from the prior stage was used as the
402 starting model for the next stage of inversion, and the final results after a total of 80 iterations
403 are shown in Fig. S4.

404 For the inversion, we only used crustal Pg arrivals, because this part of data has the most
405 linear behaviour in FWI and the wide-aperture data is sensitive to both the upper- and lower-
406 crustal structures. We didn't apply FWI to the PmP arrivals, because of its strong nonlinearity
407 around critical angles. A time-window of 0.5 s was applied to the OBS gathers, by muting the
408 data before 0.2 s, and after 0.3 s of the picked Pg travel times, to reduce the influence of
409 noise, and to isolate Pg arrivals from the other seismic events. A careful visual inspection was
410 then performed to further mute data at far offsets when the Pg, PmP and Pn arrivals overlap,
411 to reduce potential interference from Moho and mantle related seismic phases in the time
412 window. Since the Pg arrivals do not have information for updating the S-wave velocities, we
413 updated the P-wave velocity model only, with the S-wave velocity model derived from the P-

wave velocity using Brocher's regression fit[40]. The finite-difference modelling algorithm used a grid spaced at 20 m for both the horizontal and vertical directions, which can ensure the accuracy for propagating P waves with frequency range below 15 Hz. Considering the sparse distribution of OBS on the seafloor, a gaussian smoothing operator (4 km and 0.4 km in the horizontal and vertical directions, respectively) was applied to the gradient for gradient regularisation.

Source wavelet for wave equation modelling was estimated by stacking near-offset free-surface multiples of water waves[37], thanks to a good separation between water waves and seafloor-related scatterings in their free-surface multiples. An amplitude scaling factor was then estimated by comparing the field and synthetic Pg waveforms at near offsets.

Velocity anisotropy was not taken into consideration for the FWI in the present study. Although oceanic crust contains highly anisotropic minerals, their random orientation makes the oceanic crust nearly isotropic, which is supported by evidence from Hole 735B for the lower crust[30]. Studies near the ridge axis indicate anisotropy of 1%-2% at the top 3 km depth on the MAR[3]. The observed anisotropy is attributed to vertical cracks aligned with the ridge axis, and decreases fast off-axis over 5-10 km. Therefore, we consider the influence of anisotropy from upper and lower crust between 7-12 Ma negligible.

In order to heighten the salient features of the results from trace-normalised (Fig. S3) and true-amplitude (Fig. S4) FWI, besides the velocity models, we also show the velocity anomalies (the difference between the tomographic and the FWI models) as well as the vertical velocity gradients. For example, the velocity anomaly from the trace-normalised FWI highlights the large-scale velocity variations between the upper and lower crust (Fig. S3b), whereas the vertical velocity gradient from the true-amplitude FWI enhances the layered structures in the lower crust (Fig. S4c), therefore these figures are presented in Fig. 2.

Fig. S5 shows one-dimensional (1-D) velocity-depth profiles below basement between 112 km and 192 km distance along the profile from the tomographic and FWI velocity models. One can observe that there is a wider variation in velocity both in the upper and lower crust as compared to the tomographic results, with layering in the lower crust along the whole model, although the depths of these layers vary along the profile. A subset of two (1-D) velocity-depth profiles are shown in Fig. S6, with the interpreted boundaries of Layer 2A/2B and 2/3. Figs. S7 to S10 show seismic waveforms for the observed data, the initial synthetic seismograms computed using the tomographic model, and synthetic seismograms from the inverted FWI model, indicating much improved waveform match between the observed and synthetically computed data after FWI when compared with the tomographic results. Waveform fitness from FWI at far offsets is generally better than that at relatively near offsets; the reasons could be that small anomalies in the upper crust is not well resolved by sparse OBS data, and there are fewer constraints for the topmost crust from the Pg arrivals. The norm-2 misfit after FWI was reduced by 36%.

Resolution and uncertainty synthetic studies

In order to gain confidence in our results, especially for the layered structures in the lower crust, we performed several numerical tests by modifying the velocity model with different scenarios of anomalies, and then applied FWI using the same source and receiver positions and frequency ranges of the data as in the actual observation, and the same inversion parameters. We also tested the potential influence of Moho reflections (PmP).

In the first of these tests, we modified the velocity model from FWI starting from 5.8 km depth to the bottom of the model (Fig. S11), by replacing the layering structures with the corresponding tomographic model in order to see if the layered structures in the lower crust are required by the data and not due to smearing of the structures in the upper crust. Fig. S13a

462 shows a comparison of synthetic seismograms using the modified model and field data,
463 without layering in the lower crust; larger waveform misfit than Fig. 3b can be observed at
464 far (larger than 20 km) offsets, the propagation paths of which sample the lower crust. We
465 used the modified model as the starting model for FWI. The inverted model is shown in Fig.
466 S12 with remarkable similarity to Fig. S4; the waveform match is much better in Fig. S13b
467 than Fig. S13a for far offsets. This test suggests that the layered structure in the lower crust is
468 required for explaining the crustal Pg arrivals in the data.

469 Then we wanted to estimate the size of the anomaly that could be recovered using our FWI
470 settings. We began with checkerboard tests. Although not comprehensive, this is a succinct
471 and computationally efficient approach to demonstrate the resolution of FWI using available
472 data, therefore has been widely used for studying inversion problems. We generated synthetic
473 models by adding 8% positive and negative Gaussian-shaped velocity anomalies to the
474 tomographic velocity model. Fig. S14a shows the true velocity anomalies; each of the
475 Gaussian anomalies is 10 km long and 1 km thick. The perturbed velocity model was then
476 used for generating the 'observed' data for the inversion. We used the unperturbed
477 tomographic model as the starting model for the FWI to see how well these perturbations can
478 be recovered. The same procedure was applied for a second checkerboard test, with the only
479 difference being that the Gaussian anomalies have 0.5 km thickness (Fig. S15a). The inverted
480 velocity anomalies in Figs. S14b and S15b show good match with the true models, with
481 resolution for both the upper and lower crust on the scale of 10 km laterally and 500 m
482 vertically, consistent with OBS spacing and the frequency content of the data.

483 The next set of tests were to see what kind of layered structures in the lower crust that could
484 be resolved from the FWI. Five synthetic studies were performed. We perturbed the velocity
485 model, by adding five types of layered velocity anomalies shown in Figs. S16a-S20a,

respectively. The layering model in Fig. S16a contains alternating high and low velocity anomalies of ± 200 m/s with 500 m layer thickness; Fig. S17a contains high and low velocity anomalies of ± 200 m/s with a transitional gradient of 1 s^{-1}; the velocity anomalies in Fig. S18a correspond to the gradational layering with 500 m thickness for each layer, where the velocity increases linearly to 350 m/s and then sharply decreases to the background velocity at its base; the layering model in Fig. S19a are step-wise positive velocity anomalies with 500 m layer thickness, with a velocity increase of 200 m/s; finally, the layering model in Fig. S20a is a low velocity anomaly of - 300 m/s and 400 m thickness with a Gaussian-shape transition boundary.

Because of the band-limited frequency of the data, a smoothed version of the models in Figs. S16b-S20b were recovered by FWI. These tests provide evidence that the wide-aperture Pg arrivals are capable of constraining the layering structure for high and lower velocity anomalies (Figs. S16, S17, S20). The inverted model in Fig. S18b shows the increasing velocity pattern, although unable to reconstruct the sharp step boundaries. Fig. S19 indicates that the gradational layering structure cannot be resolved with high resolution by crustal Pg arrivals; instead, an average model is obtained. There are inversion artifacts in the vicinity of inverted anomaly boundaries, arising from the side lobes of seismic data. Fig. S21 shows velocity-depth functions at 168 km distance from Figs. S16-S20, highlighting the above points, and indicates that the layering velocity model in the lower crust can be well resolved and is required by the field OBS data.

We also tested if the layering in the lower crust could be introduced by the potential presence of the Moho (PmP) reflections in the windowed data containing mainly crustal Pg arrivals. We used the velocity model with Moho (Fig. S22a)[13] for generating the 'observed' data. For FWI, the velocity model after removing the Moho and upper mantle (Fig. S22b, the velocities

of these parts were replaced by velocities immediately above the Moho) was used as the starting model. A larger time window, between 0.2 s before and 0.5 s after the picked Pg travel times, than that for field data FWI, was used for including both the Pg and PmP arrivals. Fig. S23 shows the inverted velocity model, the velocity anomaly (the difference between the inverted model and the starting model), and the vertical velocity gradient. The PmP arrivals focused around Moho depths as expected, with weak artifacts in the crust. The velocity anomalies contain mainly positive values, with negative sidelobes at crustal base arising from the band-limited nature of seismic data. In a second test, we used the same window size as for field data FWI, for containing mainly the Pg arrivals for inversion. The inversion results are shown in Fig. S24. We observed weaker anomalies around the crustal base, indicating that the windowed data may contain certain PmP arrivals at far offsets, but their influence for the observed crustal layering is limited. These tests confirm that the Moho reflection is unlikely attributed to the layering structures in the lower crust, especially for those away from the base of crust; and the layering model in the lower crust away from the crustal base represents real features of the sub-surface.

Voigt-Reuss-Hill averaging for rock property modelling

In order to shed light on the types of rocks that can produce velocities comparable to those estimated from the FWI study, we estimated velocities for rocks commonly present in the lower crust. Voigt-Reuss-Hill (VRH) averaging[41] is a common and simple approach for computing the effective elastic moduli of rock from the volume fractions and elastic properties of their mineral constituents. Evidence[30-33] from IODP/ODP drilling and ophiolite show that the gabbroic rocks of the lower crust are mainly composed of olivine (Ol), clinopyroxene (Cpx), and plagioclase (Pl). Therefore, we calculated the P-wave velocities using different combinations of Ol, Cpx and Pl volume fractions. The elastic moduli and

densities[42] of the three mineral components shown in Table S1. We expect the velocities to increase with increasing Ol or Cpx, and decrease with increasing Pl. By varying the volume fractions of different components, we found a velocity variation of 200-400 m/s (± 100-200 m/s, Table S2), similar to those observed from the FWI. Pyroxene may play a more important role in increasing the velocities of gabbro than Ol, because the properties of Ol can get more easily altered leading to low effective densities and elastic moduli[33]. In the case of the properties of Ol being altered in our study area, similar amount of alternation of Cpx volume fraction can produce the P-wave velocity variations as observed in the FWI model, because the properties of Ol and Cpx are relatively close.

Data availability

The raw OBS data used for this study is stored at the PANGAEA Data center https://doi.pangaea.de/10.1594/PANGAEA.914912. The processed OBS data and the derived velocity models can be accessed at https://zenodo.org/deposit/4390552.

Code availability

The code for travel-time tomography and full waveform inversion can be accessed upon reasonable request from Singh.

Acknowledgements

The OBS data were acquired during the LITHOS-iLAB experiment on board the German R/V Maria S. Merian in 2017. We thank Dr Lydéric France for the discussion on ODP Hole 735B. This project was funded by the European Research Council Advanced Grant agreement No. 339442 TransAtlanticILAB. The cruise with the ID MSM69 was funded by

the German Science Foundation (DFG). This research was funded by the Deep Earth Imaging Future Science Platform, CSIRO. This work was supported by resources provided by the Pawsey Supercomputing Centre with funding from the Australian Government and the Government of Western Australia. We also thank the computational resources supported by S-CAPAD at IPG Paris. The maps were plotted using open software GMT 6.0.0, and the other figures were created using open software Python 2.7 with Matplotlib 3.1.0.

Author contributions

P.G. performed data processing and full waveform inversion of the OBS data, analysed the results, and wrote the paper; S.C.S. participated in the OBS data acquisition, designed and supervised the project, interpreted the results, and wrote the paper; V.A.V. participated in the OBS data acquisition, performed data processing and travel-time tomography; I.G. led the OBS data acquisition; E.S. analysed the results.

Competing interest declaration

The authors declare no competing interests.

Additional information

Supplementary information is available for this paper. Correspondence and requests for materials should be addressed to Guo.

37. Guo, P., Singh, S. C., Vaddineni, V. A., Visser, G., Grevemeyer, I., & Saygin, E. Nonlinear full waveform inversion of wide-aperture OBS data for Moho structure using a trans-dimensional Bayesian method. *Geophys. J. Int.* **224**, 1056-1078 (2021).

577 38. Tarantola, A. Inversion of seismic reflection data in the acoustic approximation. *Geophys*.
578 **49**, 1259-1266 (1984).
579 39. Van Avendonk, H. J., Harding, A. J., Orcutt, J. A., & McClain, J. S. A two- dimensional
580 tomographic study of the Clipperton transform fault. *J. Geophys. Res. Solid Earth* **103**,
581 17885-17899 (1998).
582 40. Brocher, T. M. Empirical relations between elastic wavespeeds and density in the Earth's
583 crust. *Bull. Seismol. Soc. Am.* **95**, 2081-2092 (2005).
584 41. Hill, R. The elastic behaviour of a crystalline aggregate. *Proc. Phys. Soc., A.* **65**, 349
585 (1952).
586 42. Sobolev, S. V., & Babeyko, A. Y. Modeling of mineralogical composition, density and
587 elastic wave velocities in anhydrous magmatic rocks. *Surv. Geophys.* **15**, 515-544 (1994).